AIAA Aviation Forum and ASCEND co-located Conference Proceedings
21 - 25 July 2025, Las Vegas, Nevada
AIAA AVIATION FORUM AND ASCEND 2025
10.2514/6.2025-3529

DNS and Experimental Study of Shock Wave/Turbulent Boundary Layer Interaction over a Mach 6.32 Hollow-Cylinder/Flare

Dhiman Roy*, Mateus Schuabb †, Matthew Aultman ‡, and Lian Duan §
The Ohio State University, Columbus, OH 43210, USA

Ben Segall ¶, Tim Keenoy ‖, Jaden Kokinakos **, and Nicholaus Parziale ††
Stevens Institute of Technology, Hoboken, NJ, 07030, USA

Ahsan Hameed ‡‡
U.S. Air Force Research Laboratory, Wright-Patterson AFB, OH 45433

This study presents a combined direct numerical simulation (DNS) and experimental investigation of shock wave/turbulent boundary layer interaction (SBLI) over a hollow-cylinder/flare (HCF) configuration at Mach 6.32, with a flare angle of $34°$. The DNS replicates conditions from the Stevens Shock Tunnel, with matched freestream and wall temperature conditions ($Re^u_\infty/m = 13.86 \times 10^6$, $T_w/T_r = 0.54$). Detailed comparisons of DNS against experiments are made. Upstream of the interaction, the simulation shows excellent agreement in mean velocity profiles and Morkovin-scaled turbulence intensities with Stevens' experiment, as well as with other flat-plate data in the literature. Within the flare-induced SBLI region, the DNS captures key features of separation, reattachment, and shock-induced surface loading. Instantaneous schlieren images from the DNS closely match the experimental schlieren, capturing the structure and dynamics of shock motion and the evolving separation bubble. Additionally, wall pressure signals from the DNS align well with Kulite measurements, with improved agreement observed after applying low-pass filtering to account for sensor's effective bandwidth.

Nomenclature

C_f	=	wall skin friction coefficient, $C_f = \tau_w/(0.5\rho_\infty U_\infty^2)$, dimensionless
C_h	=	wall heat flux coefficient, $C_h = q_w/[\rho_\infty c_p U_\infty (T_r - T_w)]$, dimensionless
C_p	=	pressure coefficient, $C_p = p_w/(0.5\rho_\infty U_\infty^2)$, dimensionless
D	=	cylinder diameter, m
H	=	shape factor, $H = \delta^*/\theta$, dimensionless
L	=	model length from leading edge to flare corner, m
L_{sep}	=	separation length in the streamwise direction, m
L_x	=	domain size in streamwise direction, m
M	=	Mach number, dimensionless
$(N_x,\ N_\phi,\ N_r)$	=	number of grid points in streamwise, azimuthal, and radial (wall-normal) direction
Pr	=	molecular Prandtl number, $Pr = 0.71$, dimensionless
$Re_{\delta 2}$	=	Reynolds number based on momentum thickness and wall viscosity, $Re_{\delta 2} = \rho_\infty u_\infty \theta/\mu_w$, dimensionless

*Graduate Student, Department of Mechanical and Aerospace Engineering
†Graduate Student, Department of Mechanical and Aerospace Engineering
‡Postdoctoral Scholar, Department of Mechanical and Aerospace Engineering, Member, AIAA
§Professor, Department of Mechanical and Aerospace Engineering, Associate Fellow, AIAA
¶Graduate Student, Department of Mechanical Engineering
‖Graduate Student, Department of Mechanical Engineering
**Graduate Student, Department of Mechanical Engineering
††Professor, Department of Mechanical Engineering, Associate Fellow, AIAA.
‡‡Postgraduate Scholar, NRC Research Associate

Re_τ	=	Reynolds number based on shear velocity and wall viscosity, $Re_\tau = \rho_w u_\tau \delta/\mu_w$, dimensionless
Re_τ^*	=	semilocal Reynolds number, $Re_\tau^* = \sqrt{\tau_w/\rho_\infty}\delta/\nu_\infty$, dimensionless
Re_θ	=	Reynolds number based on momentum thickness and freestream viscosity, $Re_\theta = \rho_\infty u_\infty \theta/\mu_\infty$, dimensionless
T	=	temperature, K
T_f	=	time spanned to accumulate statistics, s
T_r	=	recovery temperature, $T_r = T_\infty[1 + 0.89(\gamma - 1)M_\infty^2/2]$, K
U_∞	=	freestream velocity, m/s
c_p	=	heat capacity at constant pressure, J/(kg·K)
q_w	=	wall heat flux, W/m^2
u	=	streamwise velocity, m/s
u_τ	=	friction velocity, $u_\tau = \sqrt{\tau_w/\overline{\rho}_w}$, m/s
u_τ^*	=	density weighted velocity scale, $u_\tau^* = u_\tau\sqrt{\overline{\rho}_w/\overline{\rho}}$, m/s
w	=	wall-normal velocity, m/s
z_τ	=	viscous length, $z_\tau = \nu_w/u_\tau$, m
z_τ^*	=	semilocal length scale, $z_\tau^* = \overline{\mu}/(\overline{\rho}u_\tau^*)$, m
δ	=	boundary layer thickness (based on 99% of the freestream velocity), m
γ	=	specific heat ratio, dimensionless
κ	=	thermal conductivity of air, W/(m · K)
μ	=	dynamic viscosity, $\mu = 1.418 \times 10^{-6} \times T^{3/2}/(T + 116.4 \times 10^{-5/T})$, kg/(m·s)
ν	=	kinematic viscosity, $\nu = \mu/\rho$, m^2/s
ω	=	angular frequency, rad/s
ρ	=	fluid density, kg/m^3
τ_w	=	wall-shear stress, N/m^2
θ	=	momentum thickness, $\theta = \int_0^\delta [\{(\rho u)/(\rho_e u_e)\}(1 - u/u_e)]dz$, m
Subscripts		
e	=	boundary layer edge condition
n	=	wall-normal direction
r	=	onset of flare region
w	=	wall condition
Superscripts		
$+$	=	variable in inner wall units, $(\cdot)^+ = (\cdot)/z_\tau$
$*$	=	variable in semilocal units, $(\cdot)^* = (\cdot)/z_\tau^*$
$\overline{(\cdot)}$	=	Reynolds averaged variable
$\widetilde{(\cdot)}$	=	Favre averaged variable, $\widetilde{(\cdot)} = \overline{\rho(\cdot)}/\overline{\rho}$
$(\cdot)'$	=	fluctuations around Reynolds averages
$(\cdot)''$	=	fluctuations around Favre averages

I. Introduction

Technology development in high-speed flight is limited by the lack of practical models that are sufficiently accurate for predicting the extreme drag and heating associated with high-speed, high Reynolds number turbulent flow in the boundary layer region, because a majority of turbulence models are based on compressible flow extensions to models that were originally developed for incompressible flow, and they have not accounted for intrinsically high-speed phenomena. The errors and uncertainties in aerothermodynamic predictions of existing turbulence models lead to overly conservative designs, resulting in heavier than necessary vehicles and degraded flight performance. Despite the increased practicality of eddy resolving simulations of wall-bounded turbulence, the design of high-speed vehicles will continue to be based on the Reynolds-Averaged Navier Stokes (RANS) framework during the foreseeable future.

For the turbulent flow separated from a curved surface, the flow physics are characterized by strong non-local, non-equilibrium effects which violate the equilibrium assumptions between production and dissipation made by most eddy viscosity models. As a result, the onset of flow separation and the separation bubble size are poorly predicted by these models even for incompressible flows [1]. At high speeds, the boundary layer in external or internal flows of a vehicle may frequently encounter shock waves generated by an adjacent or opposite surface [2]. This shock–boundary layer interaction (SBLI) can induce strong adverse pressure gradient, leading to significantly flow separation. The modeling of flow separation induced by SBLI is complicated by compressibility effects such as bulk dilation, which has been shown to distort the turbulent motions within the boundary-layer and causes a restructuring of the boundary-layer turbulence [3]. Therefore, there is a need to better understand how shock-wave-induced flow separation in the high-speed regime so that the combined effects of flow separation and compressibility can be accurately modeled for use in high-speed vehicle design.

The hollow-cylinder/flare (HCF) of interest in the present investigation pertains to that of a naturally evolving zero-pressure gradient boundary layer subject to a single external surface deflection, resulting in a large separated SBLI. Such a flow is essentially an axisymmetric analogy to the flat-plate-ramp where the flat-plate surface is offset parallel to an axis of rotation. Since a HCF geometry allows for an easier integration in the wind tunnel test section and nullifies the impact of the sides of the flat plate, it offers a fundamental and simplified platform to compare against the experimental results and to cross-validate DNS and experiment techniques.

Previous DNS of SBLI using the HCF geometry was largely focused on those in the laminar and transitional regime [4, 5], while significantly fewer studies focused on the fully turbulent regime, where the location of transition is completely upstream of separation over the hollow cylinder. The current study fills in the gap by targeting a fully turbulent SBLI over HCF at Mach 6.32 which induces flow separation, with the flow conditions and HCF geometry representative of those of the Shock Tunnel in the Stevens Institute of Technology [6, 7]. The DNS results are first compared with the experiments at Stevens to cross-validate the numerical and experimental results. The detailed numerical data is then further be post-processed to provide turbulence statistics of relevance to RANS modeling.

The paper is structured as follows: Section II provides a detailed description of the HCF model geometry, flow conditions, and details of the experimental and numerical methodologies, including the simulation setup. Section III presents and analyzes the DNS results, with direct comparisons to experimental measurements. Finally, Section IV summarizes the key findings and discusses directions for future research.

II. Flow Conditions and Methodology

The present study investigates hypersonic turbulent boundary layers over a HCF configuration at a nominal Mach number of 6.32. We employ both DNS and experiment to characterize the flow physics. The test article consists of a hollow cylinder with an outer diameter of $D = 0.102$ m and length of $L = 0.965$ m. A 34° flare section follows the cylinder, expanding to a maximum diameter of 0.203 m over 1 m length. This configuration replicates the test article used in the Stevens Shock Tunnel experiments [6, 7].

The freestream conditions, detailed in Table 1, are carefully matched between simulations and experiments. The working fluid is a mixture of nitrogen and acetone with molecular mass of 30.803 kg/kmol and specific heat ratio $\gamma = 1.4077$, modeled as a perfect gas with standard Newtonian fluid relations. The HCF model wall temperature is maintained at 295 K, yielding a wall-to-recovery temperature ratio of $T_w/T_r = 0.54$, where the recovery temperature $T_r = T_\infty[1 + r(\gamma - 1)M_\infty^2/2]$ is calculated using a recovery factor of $r = 0.89$.

Table 1 Freestream and wall conditions used in the present study for both the experiments at Stevens Shock Tunnel and the current DNS.

	M_∞	Re_∞^u (1/m)	U_∞ (m/s)	ρ_∞ (kg/m^3)	T_∞ (K)	T_w (K)
Experiment	6.32	13.86×10^6	954.9	0.063	65.25	295.15
DNS	6.32	13.60×10^6	992.4	0.063	65.25	295.00

A. Experimental Methodology

The experimental campaign over the HCF was conducted in the Stevens Shock Tunnel, as seen in Fig. 1. The experimental runs utilized a N_2 driver gas and N_2 driven gas seeded with 1.5% mole fraction acetone. The nozzle reservoir enthalpy was ≈ 0.5 MJ/kg with a unit Reynolds number of $Re_\infty^u \approx 14 \times 10^6$ m^{-1} in the test section. The driver and driven gases were separated using a double diaphragm as described in Shekhtman et al. [8]. Acetone vapor was seeded in the driven section using a volumetric bubbler following Segall et al. [6] to precisely determine the mass

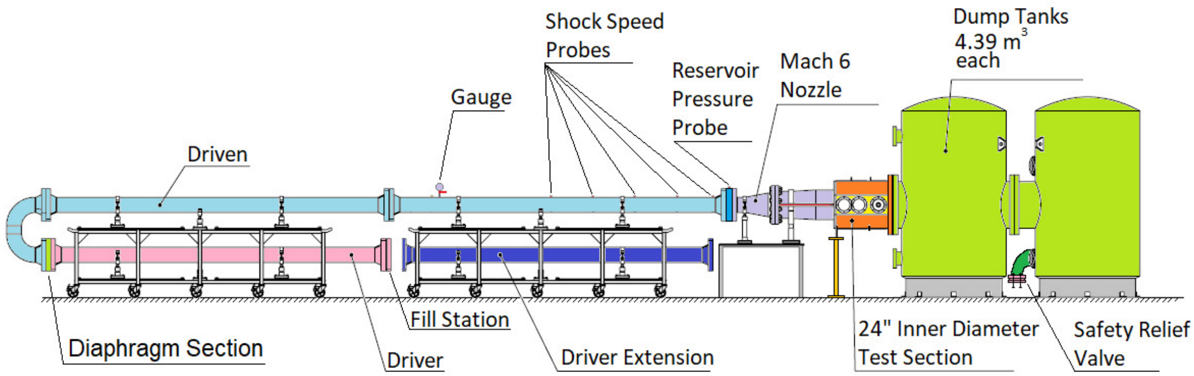

Fig. 1 Schematic of Stevens Shock Tunnel. Drawing to scale. Scale is driver tube is 5 m.

fraction. The nozzle exit diameter is 16 inch (0.406 m) with the diameter of the core flow of approximately 13 inch (0.330 m). The test article is a hollow-cylinder flare (HCF) which is 1 m long with a 4 inch (0.102 m) outer diameter hollow cylinder and a 34° flare of maximum diameter 8 inch (0.203 m). Three 40-grit sanding belt trips were placed on the test article to induce turbulence: (1) 3 inch (0.076 m) long at 1 inch (0.026 m) from the sharp leading edge; (2) 3 inch (0.076 m) long at 5.375 inch (0.137 m); and (3) 8.75 inch (0.222 m) long at 10.5 inch (0.267 m). To assess the alignment of the model, static pressure was measured on the cylinder surface at azimuthal angles of 60 and 300 degrees at $x = 0.100$ m and 0, 120, and 240 degrees at $x = 0.600$ m. All of these measurements were within 3%, which gives confidence in the alignment of the model in the test section and the uniformity of the flow. Reservoir conditions were calculated from initial gas conditions, initial pressures, and shock speed using Cantera and the Shock and Detonation Toolbox. Freestream conditions were calculated in a similar way to Segall et al. [6], Mustafa et al. [9], Segall et al. [10] and Korte et al. [11], using the pressure traces at the reservoir and Pitot pressure and assuming an isentropic expansion to iteratively find freestream Mach number M_∞.

To obtain measurements of the global flow field, two non-intrusive optical diagnostics were employed: Acetone Tagging Velocimetry (ATV) to resolve boundary layer velocity profiles, and Schlieren imaging to capture the shock and separation structures near the flare. ATV was conducted following the method of Segall et al. [6] using an externally triggered Spectral Energies Quasimodo 1200 Burst-Mode Laser System with a 4 ms burst train, 50 kHz repetition rate, and 10 ns pulse duration. The fundamental 1064 nm laser was frequency tripled to the 266 nm excitation wavelength of acetone, directed into the test section, and focused onto the HCF. The beam was oriented approximately tangent to the hollow cylinder at a point 0.85 m (33.5 inch) from the leading edge, and a coordinate transformation was used to analyze the boundary layer following the methods of Segall et al. [6]. The tagging images were captured using a Phantom TMX 7510 with a 135 mm Carl Zeiss lens with a 20 mm lens tube generating a length scale of 15 pixels/mm. In addition to velocity measurements from ATV, Schlieren imaging was performed under identical run conditions to visualize density gradients associated with shock and separation structures near the flare, as shown in Fig. 2. A 317.5 mm (12.5 inch) diameter uncoated precision parabolic mirror with a 3.175 m (125 inch) focal length was used to collimate light from a Picolas LDP-V EX-100-V4 pulsed LED with a pinhole located at the focal length to generate a ≈305 mm (12 inch) diameter cross-section. A planar mirror directed the light through a 178 mm (7 inch) diameter by 25.4 mm (1 inch) thick BK-7 window into the test section. The beam was oriented perpendicular to the flow to probe the boundary layer and the separation bubble near the flare of the HCF. A second parabolic mirror refocused the light to a minimum waist, where a knife edge was used to intercept a portion of the beam. The remaining light was focused using a free-standing plano-convex 400 mm effective focal length lens and captured using a Phantom TMX 7510.

Complementing the off-wall optical diagnostics, wall pressure measurements were obtained using an array of Kulite and PCB pressure transducers strategically distributed along the cylinder and flare surface of the HCF model, as shown in Fig. 3. The Kulite XCQ-SL-093 absolute pressure sensors (∅.096 inch), mounted on 0.096 inch diameter through holes, were used to capture low-frequency and mean pressure data along the cylinder and near the flare. These sensors provide accurate absolute pressure measurements, making them well-suited for resolving steady and quasi-steady shock and boundary layer features. In contrast, PCB 132B38 piezoelectric differential pressure transducers were used for capturing high-frequency pressure fluctuations associated with turbulent boundary layer structures and shock dynamics. These sensors, operating over a broad frequency range (11kHz–1MHz), were mounted on 0.1285 inch diameter through

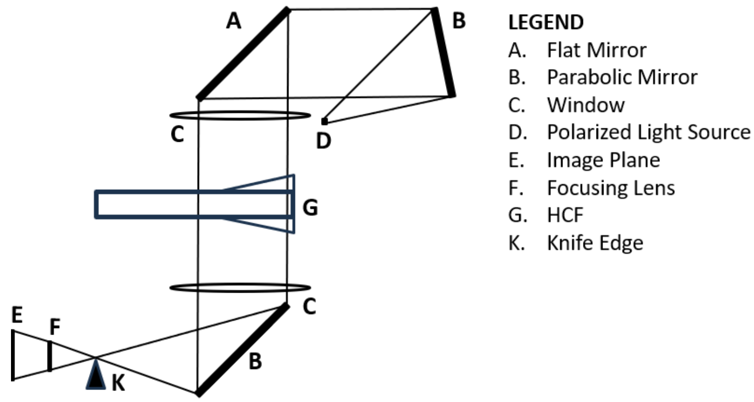

Fig. 2 Experimental Schlieren diagram.

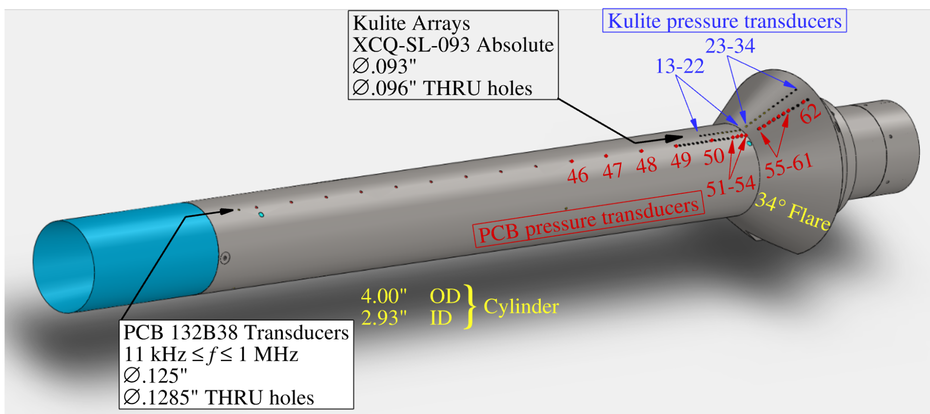

Fig. 3 Wall-pressure sensor layout on the HCF model: Kulite (blue) and PCB (red) pressure transducers.

holes. The combined Kulite and PCB array spans locations 13–61 along the HCF surface, enabling high-resolution measurements of wall pressure needed for spectral analysis and analyzing shock–boundary layer interactions.

B. DNS Methodology

To complement the experiments and provide deeper insight into boundary layer dynamics and shock–boundary layer interactions, high-fidelity DNS was performed at matching freestream conditions. The simulations offer full access to instantaneous and statistical flow fields, enabling detailed analysis of turbulence, shock-induced separation, and surface loading.

The complex flow physics over the HCF configuration requires careful numerical treatment. We employed a multiple subdomain approach that optimizes computational efficiency while maintaining high fidelity in critical flow regions. As illustrated in Fig. 4, the computational domain is partitioned into two overlapping DNS boxes, each tailored to capture distinct flow phenomena with appropriate grid resolution.

HCF, Box 1 encompasses the hollow cylinder region where the boundary layer develops over the attached surface. With an inlet boundary layer thickness of $\delta_i = 4.9$ mm and a streamwise extent of $L_x = 123\delta_i$, this box captures the fundamental turbulent boundary layer evolution. The grid employs uniform spacing in the streamwise and azimuthal directions with $\Delta x^+ = 4.7$ and $(r\Delta\phi)^+_w = 2.65$, sufficient for resolving the attached turbulent structures. In the wall-normal direction, the grid is clustered near the wall with $\Delta z^+_{n,w} = 0.47$ and gradually stretched to $\Delta z^+_{n,e} = 3.71$ near the boundary layer edge. HCF, Box 2 extends into the flare region to resolve the shock–boundary layer interaction and associated separation phenomena. This box requires significantly finer resolution to capture the steep gradients and complex flow structures that arise from the geometric discontinuity. The streamwise grid spacing varies from $\Delta x^+ = 1.6$

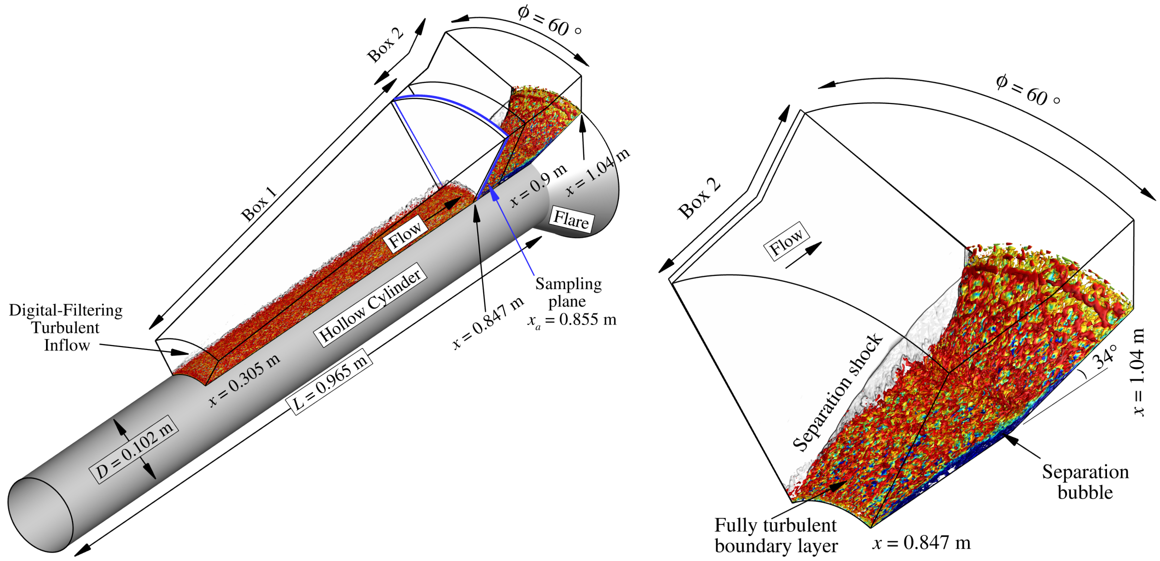

a) Full DNS domain with the HCF geometry **b) Box 2 showing SBLI region**

Fig. 4 Computational domain setup for the Mach 6.32 HCF DNS, showing an instantaneous flow visualized by iso-surface of Q-criterion. The iso-surface is colored by the streamwise velocity component, which ranges from 0 to U_∞ (blue to red).

to 3.3, with azimuthal spacing of $(r\Delta\phi)^+_w = 1.33$ and wall-normal clustering of $\Delta z^+_{n,w} = 0.13$. A smooth transition between the boxes is achieved through gradually varying grid density around the flare onset using a hyperbolic tangent function, following approaches used in previous ramp-induced shock-boundary layer interaction studies [12].

The azimuthal domain spans $\phi = 60^\circ$ to ensure adequate spanwise decorrelation of turbulent structures. At the reference sampling location, the ratio $D/\delta \approx 9.06$ corresponds to a spanwise domain size of $L_y/\delta \approx 4.74$, which allows unconstrained development of large-scale turbulent structures without artificial periodicity constraints, as confirmed in previous hypersonic boundary layer studies [5]. Detailed grid parameters are summarized in Table 2, with all spacings normalized by the local viscous length scale z_τ computed at the reference location specified in Table 3.

To assess grid sensitivity, an additional DNS was conducted over the hollow cylinder (HC) section using a coarser mesh, labeled as "HC" in Table 2. This case features larger grid spacings than the finer-resolution "HCF, Box 1" setup, with $\Delta x^+ = 6.7$, $(r\Delta\phi)^+_w = 3.97$, and $\Delta z^+_{n,w} = 4.86$. Despite the coarser resolution, the HC case showed negligible differences ($\leq 1.2\%$) in mean profiles and turbulence statistics when compared to the finer mesh, confirming that both grids are sufficiently resolved. These findings are further supported by the comparisons presented in Section III.

The in-house DNS code solves the three-dimensional compressible Navier–Stokes equations in conservative form using cylindrical coordinates. Inviscid fluxes are discretized using a seventh-order weighted essentially non-oscillatory (WENO) scheme [13] for robust shock capturing, while viscous fluxes employ a fourth-order central difference scheme. Time integration is performed using a third-order low-storage Runge–Kutta method [14], with a constant time step of $\Delta t^+ \approx 5.33 \times 10^{-3}$ for Box 1 and $\Delta t^+ \approx 1.78 \times 10^{-3}$ for Box 2. The temperature-viscosity relationship follows Keyes law [15] for Nitrogen, and thermal conductivity is computed as $\kappa = \mu c_p/Pr$ with a molecular Prandtl number of $Pr = 0.71$.

For turbulence generation at the inflow, we apply a modified digital filter turbulent inflow method for non-uniform curvilinear grids by Dhamankar et al. [16], adapted from the original digital filtering method of Klein et al. [17]. This approach superimposes artificial disturbances, generated from digitally filtered random data sets, onto predefined mean flow variables, allowing bypass of the boundary layer transition and direct turbulent structure generation within the first DNS box. Other boundary conditions include a no-slip, isothermal condition at the wall, a periodic boundary in the azimuthal direction, and an unsteady, non-reflecting boundary condition at the top boundary, based on the method of Thompson [18]. The DNS setup is suitable for capturing detailed boundary layer behavior and shock–boundary layer interaction features, as further discussed in Section III.

Turbulent statistics for HCF Box 1 are computed by first applying an azimuthal average, followed by temporal averaging over 229 snapshots, corresponding to $T_f u_\tau/\delta = 5.8$. Temporal convergence is evaluated by varying the number of snapshots and confirming minimal changes in the reported turbulence statistics. For the DNS of HCF Box 2 that includes flare-induced SBLI, the temporal snapshots obtained so far provide well-resolved near-wall dynamics and turbulence statistics. However, the current simulation duration may not be sufficient to cover multiple periods of the low-frequency unsteadiness associated with shock motion, as described by Priebe and Martín [12, 19], and the DNS run is still ongoing to collect more snapshots.

Table 2 Grid resolution and domain size for the DNS of a TBL over an HCF at Mach 6.32. The streamwise domain length is normalized by the inflow boundary layer thickness, L_x/δ_i, and the azimuthal spanwise domain size is denoted by ϕ. The grid spacing in the streamwise direction is Δx^+, while the azimuthal grid spacings at the wall and the boundary layer edge are represented by $(r\Delta\phi)^+_w$ and $(r\Delta\phi)^+_e$, respectively. Similarly, in the wall-normal direction $\Delta z^+_{n,w}$ and $\Delta z^+_{n,e}$ denote the grid spacings at the wall and at the boundary layer edge, respectively. The total data collection time is T_f. All grid spacings are reported in terms of the viscous length scale, z_τ. The values of z_τ, friction velocity u_τ, and boundary layer thickness δ are provided in Table 3.

Case	L_x/δ_i	ϕ	L_y/δ	$N_x \times N_\phi \times N_r$	Δx^+	$(r\Delta\phi)^+_w$	$(r\Delta\phi)^+_e$	$\Delta z^+_{n,w}$	$\Delta z^+_{n,e}$	$T_f u_\tau/\delta$
HC	123.0	60°	4.74	3300× 500×500	6.7	3.97	4.86	0.71	5.55	12.5
HCF, Box 1	123.0	60°	4.74	4700× 750×750	4.7	2.65	3.24	0.47	3.71	5.8
HCF, Box 2	39.8	60°	4.74	3000×1500×750	1.6 – 4.7	1.33	1.62	0.13	1.27	3.0

Table 3 Boundary layer properties at the sampling plane indicated in Fig. 4. The location $x_r = 0.0965$ m marks the onset of the flare.

Case	x/δ_i	$(x - x_r)/\delta$	Re_θ	Re_τ	$Re_{\delta 2}$	θ (mm)	H	δ (mm)	z_τ (μm)	u_τ (m/s)
HCF	176.8	-9.73	6084	421	1582	0.45	14.66	11.26	26.77	47.55

III. Results

In this section, we begin by examining the upstream turbulent boundary layer development, evaluating classical and recent velocity transformations along with turbulent statistics to assess their universality when appropriately scaled in an axisymmetric configuration. We then analyze the spatial distribution and behavior of key surface quantities such as skin friction, heat flux, and pressure as well as their temporal fluctuations within the interaction region. Finally, we examine instantaneous and time-averaged flow fields in the SBLI region, including comparisons with experimental schlieren to highlight key features and unsteady dynamics.

A. Turbulent statistics

To assess the present DNS results, Fig.5 presents mean streamwise velocity profiles transformed using four established methods: the van Driest (VD) transformation [20], the Trettel and Larsson (TL) transformation [21], the data-driven approach by Volpiani et al. [22] (V), and the total-shear-stress-based Griffin, Fu and Moin (GFM) transformation [23]. These transformations aim to collapse compressible turbulent boundary layer data onto a universal incompressible profile, enabling direct comparisons across a range of Mach numbers and wall thermal conditions. Their theoretical foundations and relative effectiveness particularly for flat plate boundary layers at freestream Mach numbers between 2.5 and 11 and wall-to-recovery temperature ratios ranging from 0.2 to 1 are comprehensively discussed in Huang et al. [24] and Szajnecki et al. [25].

Figure 5a plots the van Driest [20] transformed mean streamwise velocity u^+_{VD}, defined by an integral involving the square root of the density ratio. This transformation has historically been the standard for accounting for compressibility in wall-bounded flows. The u^+_{VD} profile aligns well with the incompressible law of the wall, exhibiting a clear logarithmic region. It closely matches the experimental data of Segall et al. [6] for a comparable HCF configuration at a similar Mach number and a slightly different wall-to-recovery temperature ratio ($T_w/T_r = 0.65$), as well as the flat plate DNS results from Zhang et al. [26], thereby validating the present DNS data in the hollow cylinder region. The TL transformation, as shown in Fig. 5b, provides improved velocity profile collapse in the near-wall region. By adjusting both velocity and spatial coordinates based on local thermodynamic and viscous properties, the TL transformation offers a more robust scaling across a range of wall temperature conditions. In Fig. 5c, the transformation proposed by Volpiani et al. [22], which leverages data-driven corrections, shows excellent agreement with the reference log law across the full boundary layer. This method is particularly effective for cooled-wall cases like those investigated here, providing more uniform scaling and better collapse across all wall-normal locations. Szajnecki et al. [25] also discussed the robustness of this transformation, noting its performance in preserving universality across Reynolds numbers and wall thermal conditions. Finally, Fig. 5d presents the GFM transformation developed by Griffin et al. [23] which accounts for total shear stress in its formulation. This method demonstrates strong agreement with the expected logarithmic behavior and exhibits consistent collapse across datasets [24, 25], suggesting its strong effectiveness in collapsing the velocity profiles.

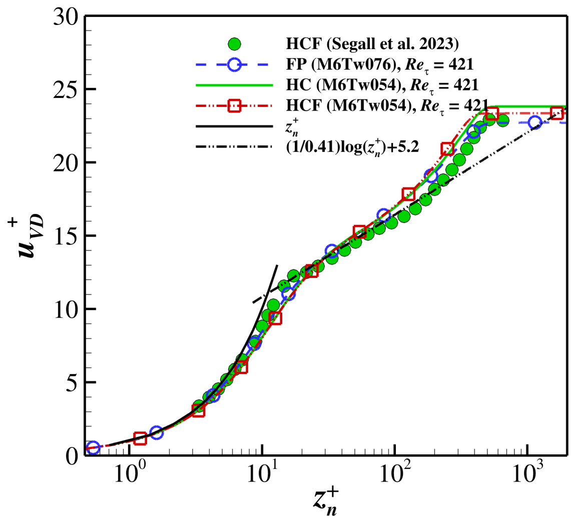

a) van Driest transformation [20] (u^+_{VD})

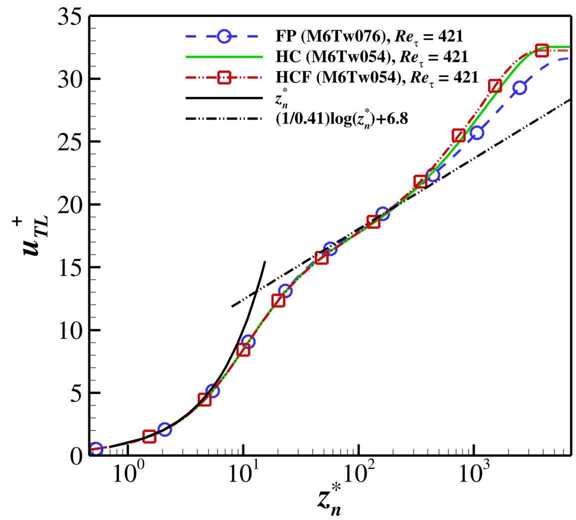

b) Trettel and Larsson transformation [21] (u^+_{TL})

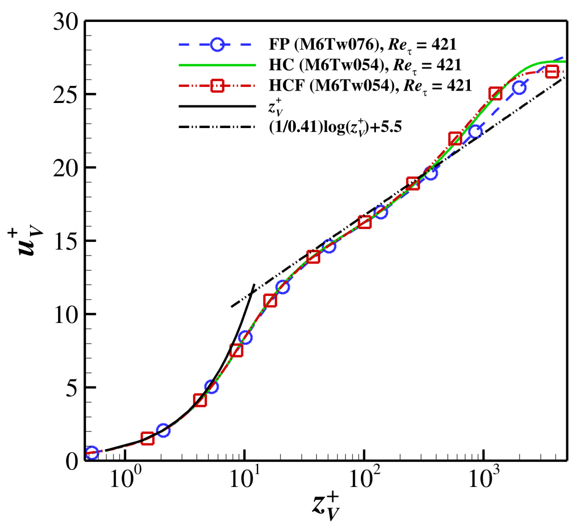

c) Volpiani et al. [22] transformation (u^+_V)

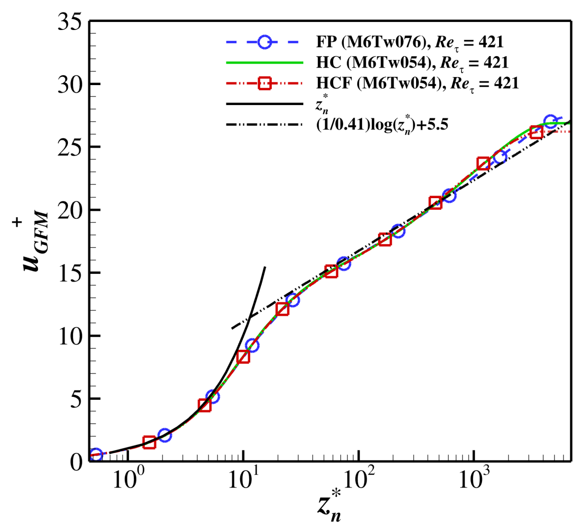

d) GFM transformation [23] (u^+_{GFM})

Fig. 5 Transformed mean velocity profiles. In Fig. 5a, u^+_{VD} obtained from the ATV measurements by Segall et al. [6] for a HCF model at $M_\infty = 6.02$ and $T_w/T_r = 0.65$ are included. M6Tw076 flat plate DNS data from Zhang et al. [26] is also included for comparison.

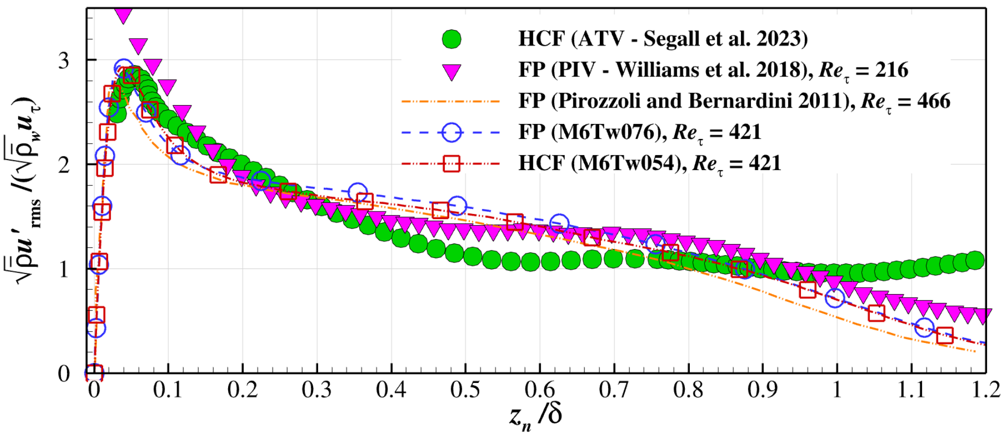

Fig. 6 Morkovin-scaled rms streamwise velocity fluctuations, $\sqrt{\bar{\rho}}\,u'_{\text{rms}}/\left(\sqrt{\bar{\rho}_w}\,u_\tau\right)$ at $(x-x_r)/\delta = -9.73$ compared with ATV data from Segall et al. [6], PIV boundary layer measurements by Williams et al. [27], and M6Tw076 flat plate DNS results from Zhang et al. [26].

Figure 6 shows the Morkovin-scaled streamwise velocity fluctuations, $\sqrt{\bar{\rho}}, u'_{\text{rms}}/(\sqrt{\bar{\rho}_w}, u_\tau)$, at $(x-x_r)/\delta = -9.73$. The peak in Morkovin-scaled streamwise velocity fluctuations consistently occurs around $z_n/\delta \approx 0.04$, with a magnitude of approximately $2.8 - 3.1$, as observed in both the present DNS and prior studies such as Duan et al. [28], Duan and Martin [29], Pirozzoli and Bernardini [30]. This alignment indicates the universality of near-wall turbulence structure in high-speed boundary layers across different configurations and wall thermal conditions. Moreover, the present DNS results exhibit excellent agreement with the DNS by Pirozzoli and Bernardini [30], flat plate DNS by Zhang et al. [26] (M6Tw076), as well as with experimental PIV data from Williams et al. [27] and ATV data from Segall et al. [6], particularly for $z_n/\delta > 0.03$, where the experimental results are less affected by near-wall measurement uncertainties. In the outer region ($0.3 \le z_n/\delta \le 1.0$), the ATV data show slightly lower fluctuation levels than DNS but follow a consistent decay trend. Beyond the boundary layer edge ($z_n/\delta > 1$), the ATV profile plateaus instead of decaying, likely due to measurement uncertainties in low signal-to-noise regions. Overall, the strong agreement within the boundary layer across DNS and experiments further supports the fidelity of the present DNS results.

The normal and shear components of the Reynolds stress tensor in semi-local coordinates at comparable friction Reynolds numbers are shown in Fig. 7. The streamwise component $\overline{\rho u''u''}/\tau_w$ exhibits the highest peak at $z_n^* \approx 15$, capturing the dominant energy containing motions aligned with the mean flow. In contrast, the azimuthal/spanwise $\overline{\rho v''v''}/\tau_w$, wall-normal $\overline{\rho w''w''}/\tau_w$, and shear $\overline{\rho u''w''}/\tau_w$ components all peak farther from the wall, around $z_n^* \approx 100$, reflecting the redistribution of turbulent kinetic energy away from the near-wall region. All components exhibit the expected growth, decay, and peak characteristics typical of canonical turbulent boundary layers. The strong agreement between the HCF and flat-plate DNS (M6Tw076), despite differences in geometry, highlights the universality of Reynolds stress behavior in hypersonic flows. Similarly, strong agreement is observed in the turbulent heat flux profiles at the selected streamwise location, as shown in Fig. 8. The streamwise component exhibits near-wall peaks at comparable locations, independent of flow conditions. Likewise, the wall-normal component peaks at similar positions across both the Mach 6 flat-plate and hollow-cylinder/flare DNS cases, further highlighting the consistency of turbulent transport behavior across geometries.

To evaluate grid sensitivity, we compared the "HCF, Box 1 DNS" with results from the additional "HC" DNS. As shown in Figs. 5, 7, and 8, the profiles from both cases exhibit excellent agreement, with only minor differences ($\le 1.2\%$) observed in mean velocity, Reynolds stress and turbulent heat flux profiles. This consistency indicates that the both grids adequately capture the boundary layer development and the essential flow physics upstream of the shock–boundary layer interaction region.

The skin friction coefficient $C_f = \tau_w/0.5\rho_\infty u_\infty^2$, wall heat flux coefficient $C_h = q_w/[\rho_\infty c_p U_\infty(T_r - T_w)]$, and pressure coefficient $C_p = p_w/0.5\rho_\infty u_\infty^2$ are fundamental surface parameters that directly reflect the aerodynamic and thermal loading experienced by a vehicle in high-speed flows. These quantities are critical for analyzing boundary layer behavior, shock-induced separation, and reattachment, and are essential for the design of thermal protection systems, drag estimation, and structural durability in hypersonic vehicles. Figure 9 presents the streamwise distributions of these three coefficients within the shock–boundary layer interaction region. Open symbols mark the separation and

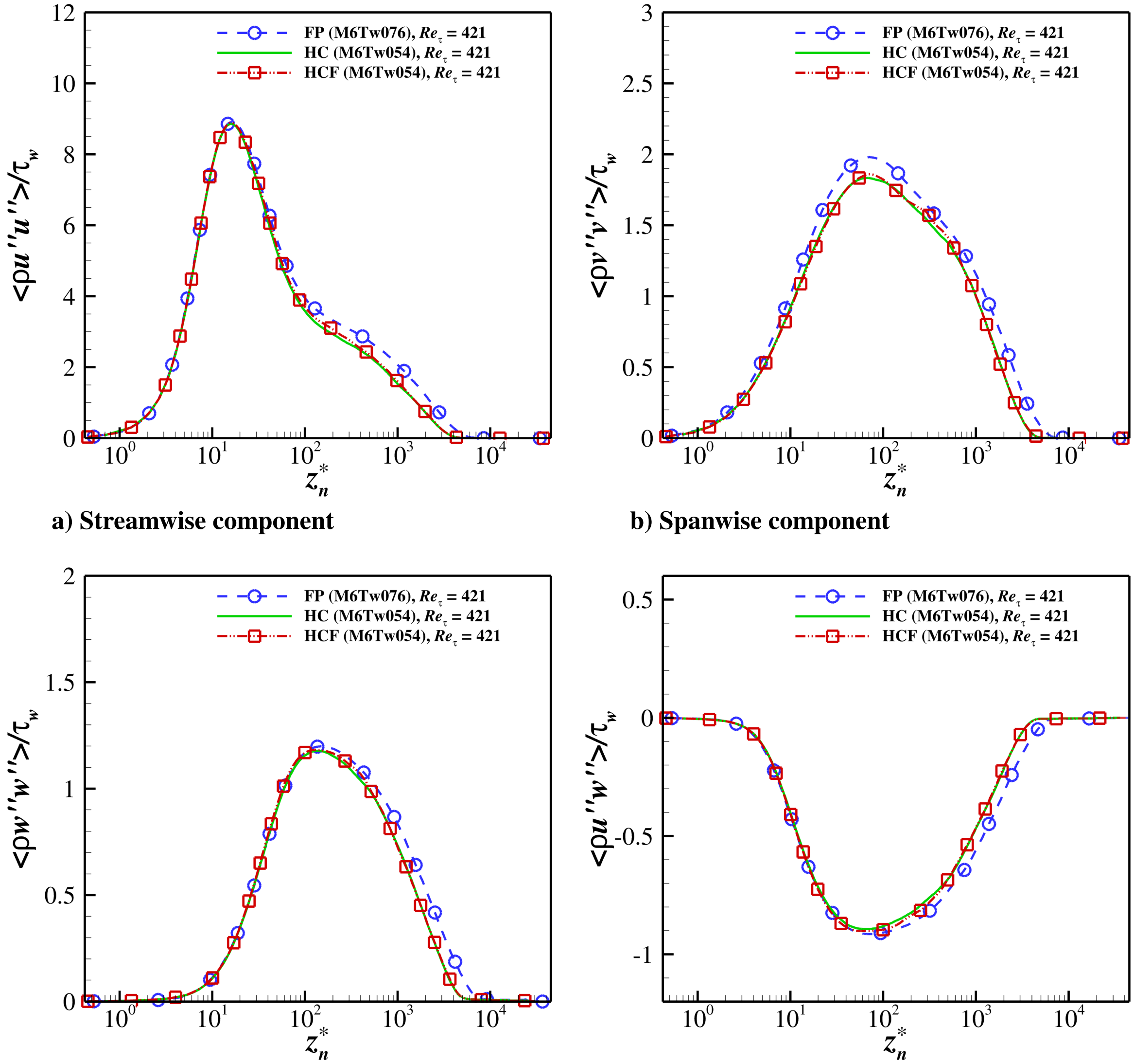

a) Streamwise component

b) Spanwise component

c) Wall-normal component

d) Shear component

Fig. 7 Comparison in Reynolds stress components $\overline{\rho u_i'' u_j''}/\tau_w$ **at** $(x - x_r)/\delta = -9.73$**.**

reattachment points, which are identified by the upstream and downstream zero-crossings of C_f, respectively. The separation length, L_{sep}, is measured as the distance between these points along the streamwise direction. Each panel also includes an enlarged view near the flare onset. The skin friction coefficient C_f in Fig. 9a shows a characteristic trend associated with flow separation and reattachment. Upstream of the interaction, C_f gradually decreases, followed by a sharp drop near the separation point where it becomes negative, reaching a minimum in the separation bubble. A second local minimum is observed just downstream of the flare onset, indicating a fully separated flow. The subsequent rise in C_f indicates reattachment and recovery of the boundary layer. The existence of two local minima in C_f is a well-known signature of strong interaction and is consistent with previous findings in both compression corner and axisymmetric flare flows [19, 31, 32]. In Fig. 9b, the wall heat flux coefficient C_h closely follows the flow separation and reattachment behavior. Within the separation region, heat transfer remains relatively low due to the weakened wall-normal gradients. Just after the flare onset, C_h rises sharply, marking a region of intense thermal loading where the boundary layer reattaches at the reattachment point and forms a local peak. This post-reattachment peak is a well-known feature in SBLI and often dictates the critical heating location, making it especially important from a design perspective. Figure 9c shows the surface pressure coefficient C_p. The pressure stays nearly constant upstream, then

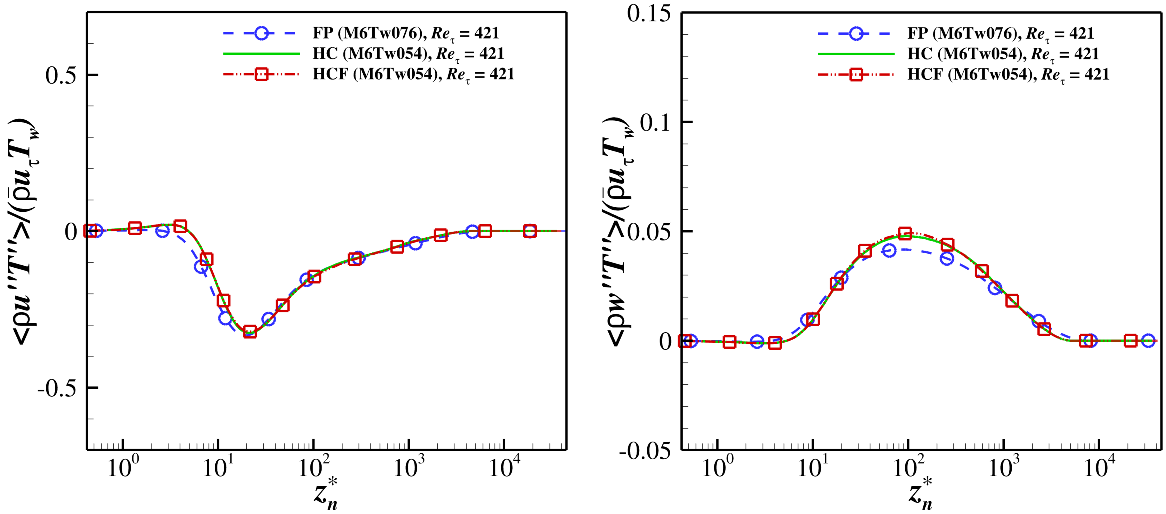

a) Steamwise component

b) Wall-normal component

Fig. 8 Turbulent heat flux for the HCF at $(x - x_r)/\delta = -9.73$ compared with flat plate DNS results.

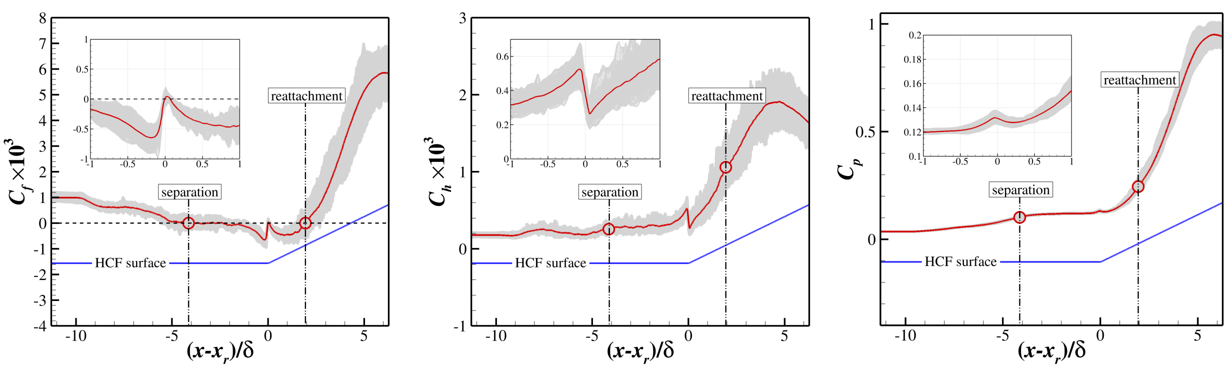

a) Skin friction coefficient

b) Wall heat flux coefficient

c) Pressure coefficient

Fig. 9 Distributions of key surface quantities within the shock–boundary layer interaction region. The shaded area shows the azimuthal variations. Open symbols shows the separation and reattachment points.

rises sharply across the shock, forming a pressure plateau inside the separation zone driven by the adverse pressure gradient. A steeper increase follows near reattachment, reflecting flow acceleration and surface compression. This also is characteristic of strong shock–boundary layer interaction and aligns well with trends observed in ramp and flare flows [31, 32]. In all three panels, the shaded regions represent azimuthal variations in the DNS data, indicating the inherent three-dimensionality of the interaction.

Figure 10 compares the mean wall pressure $\bar{p}_w/\bar{p}_{w,1}$ and RMS wall pressure fluctuations $p'_{w,\mathrm{rms}}/\bar{p}_{w,1}$ along the streamwise direction in the shock–boundary layer interaction (SBLI) region. The mean pressure profile (Fig. 10a) from DNS closely follows the trend captured by Kulite measurements, showing a gradual rise upstream of the interaction and a sharp pressure increase near $(x - x_r)/\delta \approx 2$, corresponding to the shock-induced pressure rise. In the separated flow region ($-4 \lesssim (x - x_r)/\delta \lesssim 2$), the DNS mean pressure agrees with the experimental measurements within 5%. Although the DNS slightly overpredicts the peak pressure following reattachment, the spanwise-averaged temporal variation remains well within the experimental range, demonstrating strong overall consistency between simulation and measurement.

In Fig. 10b, the RMS pressure distribution from the DNS reveals a clear increase in wall pressure fluctuations across the interaction zone, peaking just downstream of the reattachment point. While the unfiltered DNS slightly

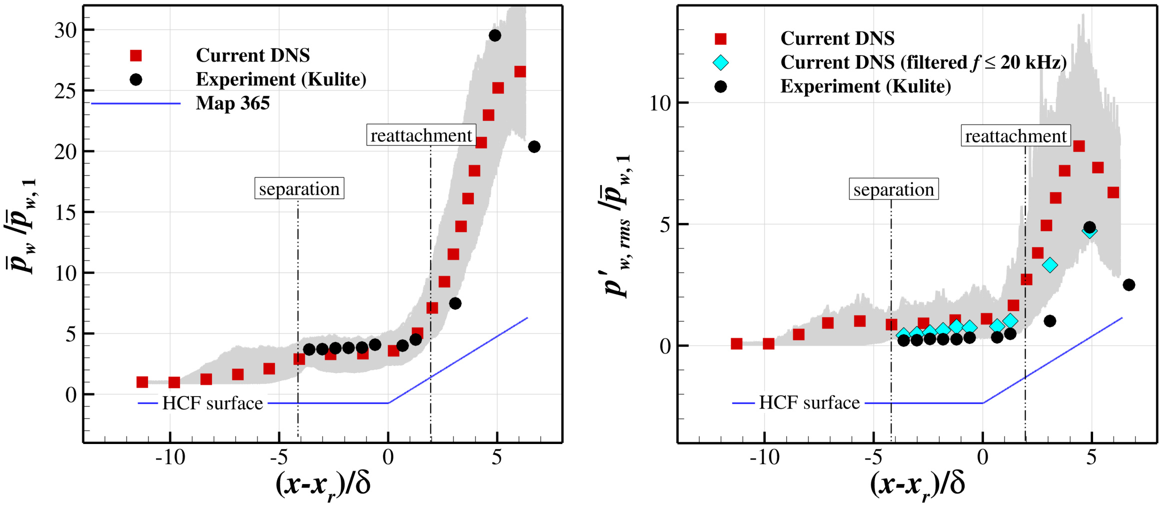

a) Mean wall pressure, $\bar{p}_w/\bar{p}_{w,1}$ **b) Root mean square, $p'_{w,\mathrm{rms}}/\bar{p}_{w,1}$**

Fig. 10 Comparison of wall pressure along the streamwise direction in the shock–boundary layer interaction region. Here, $\bar{p}_{w,1}$ is the upstream reference pressure at $(x - x_r)/\delta = -27.21$. Shaded regions indicate temporal variations in the spanwise/azimuthally averaged DNS data.

overpredicts the fluctuation levels compared to the Kulite measurements, applying a 20 kHz low-pass filter results in excellent agreement in both trend and magnitude. This consistency suggests that the dominant unsteady dynamics observed experimentally lie within the effective bandwidth of the Kulite sensors, which is typically limited to 20–25 kHz. Overall, this comparison confirms the reliability of both the DNS and experimental data, and highlights the importance of applying appropriate low-pass filtering when making direct comparisons. Matching the bandwidth of the DNS output to the sensor's effective frequency range is essential for accurately capturing and interpreting high-frequency pressure fluctuations.

B. Instantaneous and mean flow structures

To visualize and interpret the unsteady dynamics and to gain a deeper understanding of the underlying flow physics, we examine both instantaneous and mean flow structures within the interaction region. In particular, we compare numerically computed schlieren images from the DNS with time-synchronized schlieren visualizations from the experiment. This comparison helps identify the spatial and temporal evolution of key flow features such as shock waves, separation, and reattachment, providing a more complete picture of the shock–boundary layer interaction.

Figure 11 presents the instantaneous Mach number, and pressure normalized by the freestream pressure. The Mach number field in Fig. 11a clearly outlines the boundary layer, the separation bubble and the interaction region. A sharp transition from low to high Mach number occurs at the outer edge of the boundary layer, while the separation bubble is identifiable by the locally reduced Mach number near the wall, extending upstream of the flare. The shock systems are also identifiable by abrupt gradients in the Mach number. The $u/U_\infty = 0$ contour captures the instantaneous separation and reattachment locations, revealing the unsteady extent of the separation zone. The pressure field in Fig. 11b further confirms these features. A localized pressure rise is observed near the flare corner, consistent with the interaction and reattachment processes. Upstream of the flare, the low-pressure region associated with the separation bubble is evident, along with pressure disturbances that propagate along the shear layer. These unsteady fluctuations in both pressure and Mach number highlight the dynamic nature of the interaction and its influence on boundary layer behavior.

Figure 11c presents the time trace of wall pressure from the DNS at the spanwise midplane, sampled within the interaction region at $(x - x_r)/\delta = -1.81$. The figure includes three signals: the unfiltered DNS trace, a low-pass filtered DNS signal (cutoff at $f \leq 20$, kHz), and the experimental pressure signal obtained using a Kulite sensor at the same location. As expected, the raw DNS signal exhibits high-frequency content beyond the range of the experimental sensor, reflecting the broadband nature of pressure fluctuations generated by turbulence, shocks, and shear layer interactions. Once the DNS signal is filtered to match the sensor's bandwidth, it shows good agreement with the experimental data

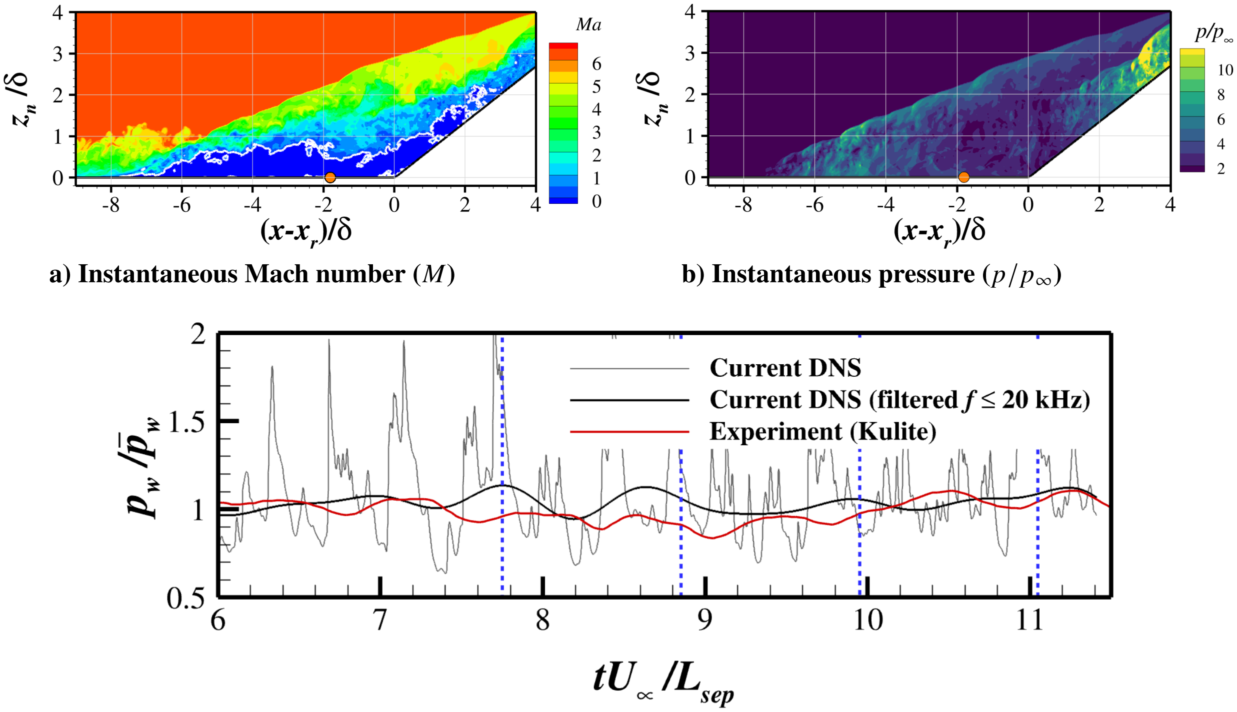

a) Instantaneous Mach number (M)

b) Instantaneous pressure (p/p_∞)

c) Time trace of p_w at $(x - x_r)/\delta = -1.81$

Fig. 11 Instantaneous visualizations for the Mach 6.32 HCF. In (a), white lines denote $u/U_\infty = 0$ isolines. In (c), the time trace of wall pressure is extracted from the spanwise midplane of the DNS domain within the interaction region at $(x - x_r)/\delta = -1.81$. The raw and low-pass filtered DNS signals ($f \leq 20$ kHz) are shown alongside the experimental (Kulite) time trace. The probe location in (c) is indicated by the filled circles in (a) and (b).

closely capturing both the amplitude and temporal spacing of the pressure peaks.

To understand the physical origins of these pressure fluctuations, we turn to Fig.12, which shows instantaneous schlieren images at four selected time instants marked on the pressure trace in Fig.11c. Each panel compares the experimentally captured schlieren frame with a numerically reconstructed schlieren visualization from the DNS. Across all four time instants, there is remarkable agreement between the simulation and experiment. Key features such as the separation shock, separation bubble, reattachment etc. are consistent in both visualizations. Of particular interest is the variation in the shock intersection location across the different frames which changes noticeably from one time instant to another, indicating unsteady motion. This unsteadiness is consistent with the large-scale pressure excursions observed in the filtered time trace. In both DNS and experimental schlieren, the intersection point oscillates, which coincides with the low-frequency "breathing" motion of the separation bubble. This phenomenon is characteristic of shock–boundary layer interactions at high Mach numbers and has been well documented in previous studies, including those by Priebe and Martín [12, 19].

Figure 13 presents the instantaneous and time-averaged surface quantities - skin friction coefficient (C_f), wall heat flux coefficient (C_h), and pressure coefficient (C_p) on the surface of the cylinder/flare within the SBLI region. The left column (panels a, c, e) displays instantaneous fields capturing the unsteady nature of the flow, while the right column (panels b, d, f) shows time-averaged quantities revealing the mean flow structure. The instantaneous C_f field in Fig. 13a displays irregular patterns with alternating regions of positive and negative skin friction, particularly within the separated flow zone upstream of the flare, indicating intermittent flow reversal and reattachment of turbulent eddies. Downstream of reattachment, where the boundary layer redevelops, the instantaneous skin friction field becomes more coherent. In the time-averaged C_f distribution (Fig. 13b), a broad region of near-zero or negative C_f values is evident upstream of the flare, showing the separated flow zone. This is followed by a sharp increase in C_f on the flare surface, indicating flow reattachment.

In Fig. 13c, the instantaneous St contours show pronounced streamwise-aligned streaks on the flare surface,

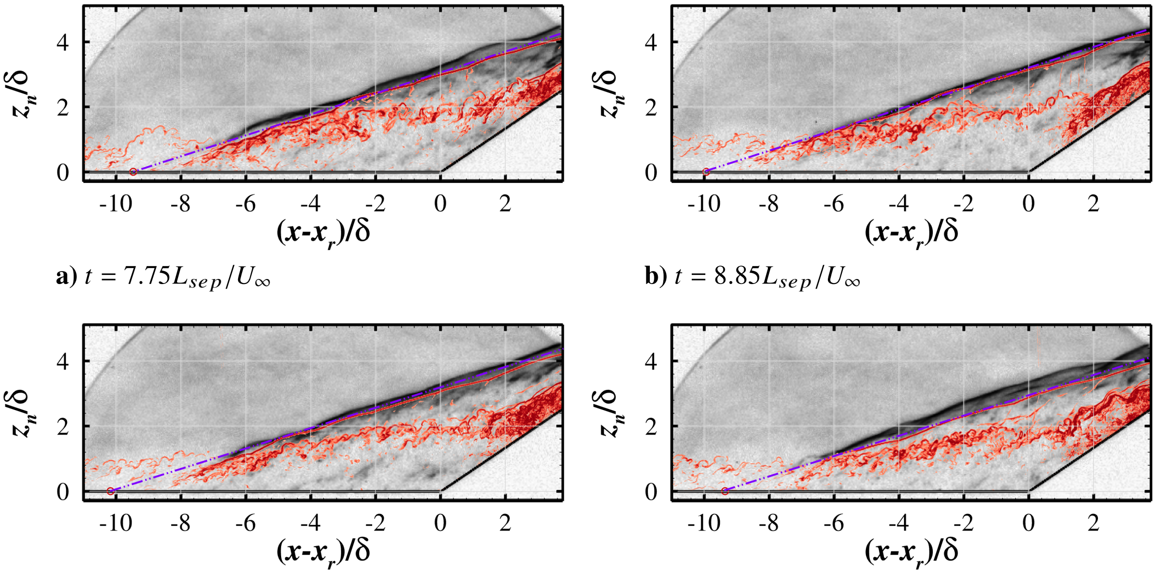

a) $t = 7.75 L_{sep}/U_\infty$ **b)** $t = 8.85 L_{sep}/U_\infty$

c) $t = 9.95 L_{sep}/U_\infty$ **d)** $t = 11.05 L_{sep}/U_\infty$

Fig. 12 Comparison of experimental Schlieren (gray) from the Stevens Shock Tunnel with numerical Schlieren (red) from the present DNS.

representing localized regions of elevated heat transfer caused by coherent turbulence structures interacting with the wall. These features are indicative of unsteady thermal loading downstream of reattachment. Similarly, the C_p field in Fig. 13e, exhibits scattered pressure patches corresponding to the fluctuating position and strength of shock waves and the separation bubble, showing the influence of low-frequency shock motion on surface pressure. The time-averaged C_h contour shows a clear peak near the reattachment region (black solid line on the flare), indicating enhanced heat transfer due to boundary layer recovery. Moreover, the time-averaged C_p field exhibits an abrupt pressure rise just downstream of reattachment, characteristic of shock-induced compression in the interaction zone.

IV. Summary and Future Work

This study presents DNS and experimental investigation of a Mach 6.32 flow over a hollow-cylinder/flare configuration, focusing on both the upstream development of the turbulent boundary layer over the hollow cylinder and the complex shock–boundary layer interaction induced by a 34° flare. The evolution of the axisymmetric turbulent boundary layer and its interaction with the flare-induced shock are investigated, with particular emphasis on velocity transformations, turbulence statistics, and surface loading. Upstream of the interaction, the boundary-layer statistics from DNS shows strong agreement with Stevens Shock Tunnel experiments and other DNS cases, including excellent collapse of mean velocity profiles and consistent trends in turbulence intensity, Reynolds stresses, and heat flux profiles. Within the interaction region, the DNS predicted instantaneous schlieren visualizations demonstrate remarkable agreement with experimental schlieren images, capturing the structure and dynamics of shock interactions and the evolving separation bubble. The mean wall pressure from the DNS shows excellent agreement with the Kulite measurements, while the RMS fluctuations also align well after applying a 20 kHz low-pass filter, which highlights the importance of accounting for the sensor's effective bandwidth in such comparisons.

Future work will focus on extending the DNS time duration to allow better characterization of low-frequency unsteadiness, particularly the shock breathing motion observed in the interaction zone. Additionally, PCB measurements will be included, which will be combined with Kulite for a more detailed comparative spectral analysis with the DNS, leveraging their complementary frequency ranges to better characterize the unsteady pressure dynamics.

Acknowledgments

The authors from OSU would like to acknowledge financial support by the Office of Naval Research (under grant N00014-23-1-2304, managed by Dr. Eric Marineau). Computational resources were provided by the DoD High Performance Computing Modernization Program and the Ohio Supercomputer Center. The authors from Stevens Institute of Technology were supported by ONR Grants, including N00014-20-1-2682, N00014-20-1-2637, N00014-23-1-2474 and N00014-24-1-2202. They thank Eric Marineau and the Office of Naval Research for sponsoring the construction and development of the Stevens Shock Tunnel. The views and conclusions contained herein are those of the authors only and should not be interpreted as representing those of ONR, the U.S. Navy or the U.S. Government.

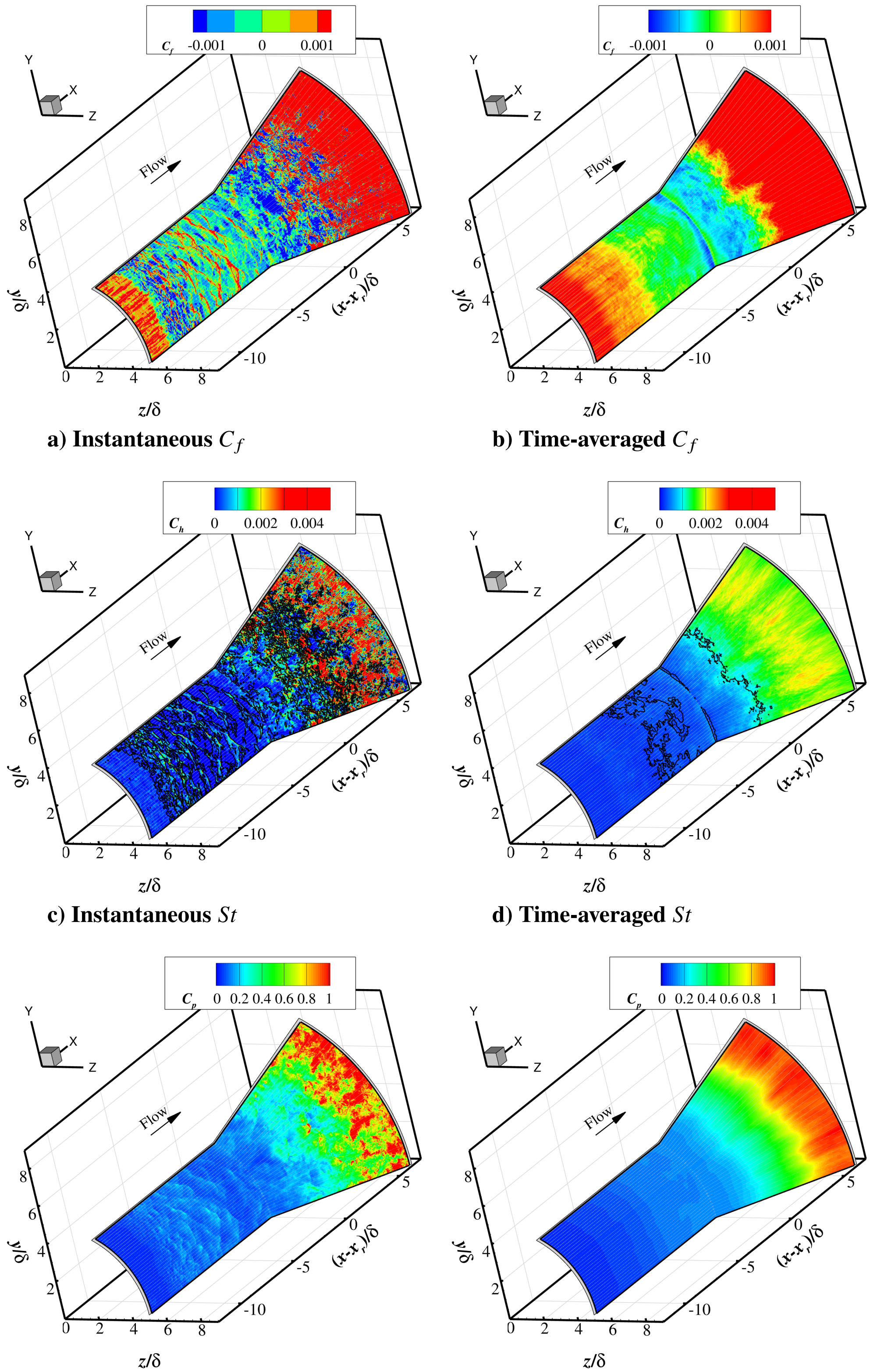

a) Instantaneous C_f b) Time-averaged C_f

c) Instantaneous St d) Time-averaged St

e) Instantaneous C_p f) Time-averaged C_p

Fig. 13 Contours of (a, c, e) instantaneous and (b, d, f) time-averaged quantities within the shock–boundary layer interaction region. Solid black lines in (c) and (d) denote $C_f = 0$ isolines.

References

[1] Wilcox, D., *Turbulence Modeling for CFD*, DCW Industries, 2006.

[2] Gaitonde, D. V., "Progress in shock wave/boundary layer interactions," *Progress in Aerospace Sciences*, Vol. 72, 2015, pp. 80–99. https://doi.org/10.2514/6.2013-2607.

[3] Tichenor, N. R., Humble, R. A., and Bowersox, R. D. W., "Response of a Hypersonic Turbulent Boundary Layer to Favourable Pressure Gradients," *Journal of Fluid Mechanics*, Vol. 722, 2013, pp. 187–213. https://doi.org/10.1017/jfm.2013.89.

[4] Lugrin, M., Beneddine, S., Leclercq, C., Garnier, E., and Bur, R., "Transition scenario in hypersonic axisymmetrical compression ramp flow," *Journal of Fluid Mechanics*, Vol. 907, 2021, p. A6. https://doi.org/10.1017/jfm.2020.833.

[5] Lugrin, M., Beneddine, S., Garnier, E., and Bur, R., "Multi-scale study of the transitional shock-wave boundary layer interaction in hypersonic flow," *Theoretical and Computational Fluid Dynamics*, Vol. 36, No. 2, 2022, pp. 277–302. https://doi.org/10.1007/s00162-021-00595-7.

[6] Segall, B. A., Shekhtman, D., Hameed, A., Chen, J. H., and Parziale, N. J., "Profiles of streamwise velocity and fluctuations in a hypersonic turbulent boundary layer using acetone tagging velocimetry," *Experiments in Fluids*, Vol. 64, No. 6, 2023, p. 122. https://doi.org/10.1007/s00348-023-03647-2.

[7] Chen, J. H., Hameed, A., Parziale, N. J., Roy, D., and Duan, L., "Spectral Analysis of Mach 6 Turbulent Boundary Layer over a Hollow Cylinder with FLDI and DNS," *AIAA Paper* 2024-2734, 2024. https://doi.org/10.2514/6.2024-2734.

[8] Shekhtman, D., Hameed, A., Segall, B. A., Dworzanczyk, A. R., and Parziale, N. J., "Initial Shakedown Testing of the Stevens Shock Tunnel," *AIAA Paper* 2022-1402, 2022. https://doi.org/10.2514/6.2022-1402.

[9] Mustafa, M. A., Parziale, N. J., Smith, M. S., and Marineau, E. C., "Nonintrusive Freestream Velocity Measurement in a Large-Scale Hypersonic Wind Tunnel," *AIAA Journal*, Vol. 55, No. 10, 2017, pp. 3611–3616. https://doi.org/10.2514/1.J056177.

[10] Segall, B. A., Shekhtman, D., Hameed, A., Chen, J. H., and Parziale, N. J., "Tagging Velocimetry in the Stevens Shock Tunnel," *AIAA paper* 2023-2337, 2023. https://doi.org/10.2514/6.2023-2337.

[11] Korte, J. J., Lafferty, J. F., Smith, M. S., Lewis, D. R., Butcher, C. W., Fredrick, N. J., Zarzecki, M., and Tatum, K. E., "Determination of Hypervelocity Freestream Conditions for a Vibrationally Frozen Nitrogen Flow," *AIAA Paper* 2021-0981, 2021. https://doi.org/10.2514/6.2021-0981.

[12] Priebe, S., and Martín, M. P., "Low-frequency unsteadiness in shock wave–turbulent boundary layer interaction," *Journal of Fluid Mechanics*, Vol. 699, 2012, pp. 1–49. https://doi.org/10.1017/jfm.2011.560.

[13] Jiang, G.-S., and Shu, C.-W., "Efficient implementation of weighted ENO schemes," *Journal of Computational Physics*, Vol. 126, No. 1, 1996, pp. 202–228. https://doi.org/10.1006/jcph.1996.0130.

[14] Williamson, J., "Low-storage runge-kutta schemes," *Journal of Computational Physics*, Vol. 35, No. 1, 1980, pp. 48–56. https://doi.org/10.1016/0021-9991(80)90033-9.

[15] Keyes, F. G., "A summary of viscosity and heat-conduction data for He, A, H2, O2, N2, CO, CO2, H2O, and air," *Transactions of the American Society of Mechanical Engineers*, Vol. 73, No. 5, 1951, pp. 589–595. https://doi.org/10.1115/1.4016342.

[16] Dhamankar, N. S., Martha, C. S., Situ, Y., Aikens, K. M., Blaisdell, G. A., Lyrintzis, A. S., and Li, Z., "Digital filter-based turbulent inflow generation for jet aeroacoustics on non-uniform structured grids," *52nd Aerospace Sciences Meeting*, 2014, p. 1401. https://doi.org/10.2514/6.2014-1401.

[17] Klein, M., Sadiki, A., and Janicka, J., "A digital filter based generation of inflow data for spatially developing direct numerical or large eddy simulations," *Journal of Computational Physics*, Vol. 186, No. 2, 2003, pp. 652–665. https://doi.org/10.1016/s0021-9991(03)00090-1.

[18] Thompson, K. W., "Time dependent boundary conditions for hyperbolic systems," *J. Comput. Phys.*, Vol. 68, No. 1, 1987, pp. 1–24. https://doi.org/10.1016/0021-9991(87)90041-6.

[19] Priebe, S., and Martin, P., "Direct numerical simulation of a hypersonic turbulent boundary layer on a large domain," *41st AIAA Fluid Dynamics Conference and Exhibit*, 2011, p. 3432. https://doi.org/10.2514/6.2011-3432.

[20] Van Driest, E. R., "Turbulent boundary layer in compressible fluids," *Journal of the Aeronautical Sciences*, Vol. 18, No. 3, 1951, pp. 145–160. https://doi.org/10.2514/8.1895.

[21] Trettel, A., and Larsson, J., "Mean velocity scaling for compressible wall turbulence with heat transfer," *Physics of Fluids*, Vol. 28, No. 2, 2016, p. 026102. https://doi.org/10.1063/1.4942022.

[22] Volpiani, P. S., Iyer, P. S., Pirozzoli, S., and Larsson, J., "Data-driven compressibility transformation for turbulent wall layers," *Physical Review Fluids*, Vol. 5, No. 5, 2020, p. 052602. https://doi.org/10.1103/physrevfluids.5.052602.

[23] Griffin, K. P., Fu, L., and Moin, P., "Velocity transformation for compressible wall-bounded turbulent flows with and without heat transfer," *Proceedings of the National Academy of Sciences*, Vol. 118, No. 34, 2021. https://doi.org/10.1073/pnas.2111144118.

[24] Huang, J., Duan, L., and Choudhari, M. M., "Direct numerical simulation of hypersonic turbulent boundary layers: effect of spatial evolution and Reynolds number," *Journal of Fluid Mechanics*, Vol. 937, 2022, p. A3. https://doi.org/10.1017/jfm.2022.80.

[25] Szajnecki, L., Roy, D., Duan, L., and Bisek, N. J., "Effect of Reynolds Number on a High-Speed Cold-Wall Turbulent Boundary Layer," *Journal of Fluid Mechanics*, 2025. Accepted for publication.

[26] Zhang, C., Duan, L., and Choudhari, M. M., "Direct numerical simulation database for supersonic and hypersonic turbulent boundary layers," *AIAA Journal*, Vol. 56, No. 11, 2018, pp. 4297–4311. https://doi.org/10.2514/1.j057296.

[27] Williams, O. J., Sahoo, D., Baumgartner, M. L., and Smits, A. J., "Experiments on the structure and scaling of hypersonic turbulent boundary layers," *Journal of Fluid Mechanics*, Vol. 834, 2018, pp. 237–270. https://doi.org/10.1017/jfm.2017.712.

[28] Duan, L., Beekman, I., and Martin, M., "Direct numerical simulation of hypersonic turbulent boundary layers. Part 2. Effect of wall temperature," *Journal of Fluid Mechanics*, Vol. 655, 2010, pp. 419–445. https://doi.org/10.1017/s0022112010000959.

[29] Duan, L., and Martin, M., "Direct numerical simulation of hypersonic turbulent boundary layers. Part 4. Effect of high enthalpy," *Journal of Fluid Mechanics*, Vol. 684, 2011, pp. 25–59. https://doi.org/10.1017/jfm.2011.252.

[30] Pirozzoli, S., and Bernardini, M., "Direct Numerical Simulation Database for Impinging Shock Wave/Turbulent Boundary-layer Interaction," *AIAA Journal*, Vol. 49, No. 6, 2011, pp. 1307–1312. https://doi.org/10.2514/1.J050901.

[31] Kaufman II, L. G., Hartofilis, S. A., Evans, W. J., Oman, R. A., Meckler, L. H., and Weiss, D., "A Review of Hypersonic Flow Separation and Control Characteristics," Technical report (asd-tdr-62-168), Grumman Aircraft Engineering Corp., Mar. 1962. Approved for public release; distribution is unlimited.

[32] Li, C., and Hao, J., "Global stability of supersonic flow over a hollow cylinder/flare," *Journal of Fluid Mechanics*, Vol. 975, 2023, p. A40. https://doi.org/10.1017/jfm.2023.865.